Thermodynamic and First-principles Assessments of Materials for Solar-driven CO₂ Splitting Using Two-step Thermochemical Cycles
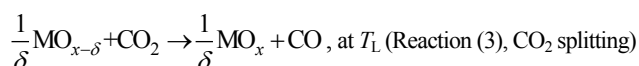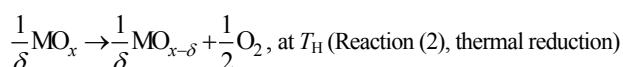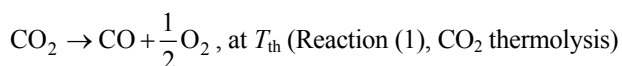
FENG Qingying, LIU Dong, ZHANG Ying, FENG Hao, LI Qiang

(School of Energy and Power Engineering, Nanjing University of Science and Technology, Nanjing 210094, China)

Abstract: Carbon-neutral fuel production by solar-driven two-step thermochemical carbon dioxide splitting provides an alternative to fossil fuels as well as mitigates global warming. The success of this technology relies on the advancements of redox materials. Despite the recognition of the entropic effect, usually energy descriptors (enthalpy of formation or energy of oxygen-vacancy formation) were used for computational assessment of material candidates. Here, in the first step, the criteria was derived based on the combination of solid-state change of entropy and formation enthalpy, and was used to thermodynamically assess the viability of material candidates. In the thermodynamic map, a triangular region, featuring large positive solid-state changes of entropy and small enough solid-state changes of formation enthalpy, was found for qualified candidates. Next, a first-principles DFT+U method was presented to fast and reasonably predict the solid-state changes of entropy and formation enthalpy of candidate redox materials, exemplified for pure and Samaria-doped ceria, so that new redox materials can be added to the thermodynamic map. All above results highlight the entropic contributions from polaron-defect vibrational entropy as well as ionic (oxygen vacancies) and electronic (polarons) configurational entropy.

Key words: carbon dioxide splitting; two-step thermochemical cycle; first principles; entropy; solar fuel

Using solar energy to convert carbon dioxide (CO₂) into carbon-neutral fuels provides an alternative to fossil fuels and mitigates global warming. In analogy to conventional chemical plants, a solar-fuel plant is able to operate overnight addressing the intermittency of solar energy. Regarding this, concentrated solar thermochemical CO₂ splitting holds promise because cost-effective and high-density heat storage can be integrated into this technology[1]. Direct CO₂ splitting by thermolysis, requires temperature as high as 3000 ℃ except for separation of oxygen from fuel products. Therefore, research converged to the two-step redox cycles based on partial reduction (or non-stoichiometric, oxygen-vacancy) and oxidation of non-volatile oxides (or redox materials), because this type of cycles features the combinations of practical operation temperature and high thermodynamic efficiency[1-3].

$$CO_2 \rightarrow CO + \frac{1}{2}O_2 \text{, at } T_{th} \text{ (Reaction (1), CO}_2 \text{ thermolysis)}$$

$$\frac{1}{\delta}MO_x \rightarrow \frac{1}{\delta}MO_{x-\delta} + \frac{1}{2}O_2 \text{, at } T_H \text{ (Reaction (2), thermal reduction)}$$

$$\frac{1}{\delta}MO_{x-\delta} + CO_2 \rightarrow \frac{1}{\delta}MO_x + CO \text{, at } T_L \text{ (Reaction (3), CO}_2 \text{ splitting)}$$

Although considerable materials[4] have been examined including ceria[5-8], ferrites[9-11] and perovskites[12-14], the state-of-the-art solar-to-chemical energy conversion efficiency was as low as ~5% for solar thermochemical CO₂ splitting[5]. Therefore, computational assessments of materials are still of great importance[15-17]. Intuitively, the thermodynamically suitable redox materials can be identified based on the fundamental concept that the change in the Gibbs free energy, ΔG, should be negative for the two cycle steps (Reactions (2) and (3)). Thereby, solid-state enthalpy and entropy of reduction excluding the contributions from gaseous species (whose thermodynamic property data is available for a wide range of conditions) can be used as the descriptors for thermodynamic assessments of redox materials. Particularly, Meredig[18] and

Shah, *et al.*[19] raised the importance of entropic effects. Unfortunately, obtaining reliable thermodynamic data, especially the reduction entropy, of redox material candidates, either computationally or experimentally is often challenging[11-12,20-24]. For example, Bork, *et al.*[12] used CALPHAD models to access or extrapolate needed thermodynamic properties of perovskites, but models with this level of sophistication are not available for many redox material candidates[2]. Michalsky, *et al.*[22] found that the Gibbs free energy for formation of many bulk oxides (equivalent to solid-state enthalpy and entropy of reduction) scaled with their oxygen-vacancy formation energy at their most stable surfaces. However, this scaling feature was only demonstrated in the stoichiometric regime. Muhich, *et al.*[11] developed an assessment method where only the enthalpy of reduction was used, but this method only worked for the assessments within the same class of materials (hercynite in their work) because the reduction entropy is approximately the same for the hercynite family.

Therefore, this study provided general descriptors and criteria for thermodynamic assessments of proposed or newly discovered redox materials, and to provide first-principles methods for fast predictions of these descriptors. Here, pure and Samaria-doped ceria were taken as benchmark materials because they own fast splitting kinetics, excellent high-temperature and cycling stability[5-8], and also provide a platform for first-principles investigations of the effects of typical defects including oxygen vacancies, polarons and dopant ions[25].

1 Thermodynamic derivation of descriptors and criteria

In this section, the descriptors was proposed, and then the criteria was derived for thermodynamic assessments of the viability of material candidates. In the derivation, complementary constraints were presented in consideration of non-stoichiometric reaction mechanism, theoretical efficiency and practical operating conditions of the solar-driven two-step thermochemical process to extend the thermodynamic framework described by Meredig and Wolvertor[18].

This study starts with the fundamental concept that the change in the Gibbs free energy, ΔG, should be negative for the two cycle steps (Reactions (2) and (3)) so that they are thermodynamically favorable. This gives Eq. (1–2).

$$\Delta G_2 = \frac{1}{\delta}(\Delta H_{f,MO_{x-\delta}} - \Delta H_{f,MO_x}) - T_H \times$$
$$\left[\frac{1}{\delta}(S_{MO_{x-\delta}} - S_{MO_x}) + \frac{1}{2}(S_{O_2,T_H} - R\ln P_{O_2})\right] \leqslant 0 \quad (1)$$

$$\Delta G_3 = \frac{1}{\delta}(\Delta H_{f,MO_x} - \Delta H_{f,MO_{x-\delta}}) + (\Delta H_{f,CO,T_L} - \Delta H_{f,CO_2,T_L}) -$$
$$T_L \times \left[\frac{1}{\delta}(S_{MO_x} - S_{MO_{x-\delta}}) + (S_{CO,T_L} - S_{CO_2,T_L})\right] \leqslant 0 \quad (2)$$

where ΔH_f represents the enthalpy of formation, S represents entropy, P represents pressure (kPa) and R is the ideal gas constant. Solid-state entropy and solid-state enthalpy of formation are assumed to be temperature-independent. Observed from Eq. (1) and (2), solid-state change of entropy, ΔS_{solid}, and change of enthalpy of formation, ΔH_{solid}

$$\begin{cases} \Delta S_{solid} = \frac{1}{\delta}(S_{MO_{x-\delta}} - S_{MO_x}) \\ \Delta H_{solid} = \frac{1}{\delta}(\Delta H_{f,MO_{x-\delta}} - \Delta H_{f,MO_x}) \end{cases} \quad (3)$$

depend on the redox material, while the rest quantities for gaseous species are independent and were well documented[26]. Therefore, ΔS_{solid} with unit of $J\cdot(0.5\ mol\ O_2)^{-1}\cdot K^{-1}$ and ΔH_{solid} with unit of $kJ\cdot(0.5\ mol\ O_2)^{-1}$, defined in Eq. (3), were used as descriptors for thermodynamic assessments in this work. By substituting Eq. (3) into Eq. (1) and (2), Eq. (4–5), two of the assessment criteria, are obtained.

$$\Delta H_{solid} \leqslant T_H\left(\Delta S_{solid} + \frac{1}{2}S_{O_2,T_H} - \frac{1}{2}R\ln P_{O_2}\right) \quad (4)$$

$$\Delta H_{solid} \geqslant (\Delta H_{f,CO,T_L} - \Delta H_{f,CO_2,T_L}) - T_L(S_{CO,T_L} - S_{CO_2,T_L} - \Delta S_{solid}) \quad (5)$$

In the next step, thermodynamic principles are applied to analyse the solar-to-chemical (STC) energy conversion efficiency of the two-step thermochemical process to provide complementary criteria. STC efficiency, $\eta_{STC} = \eta_{STT} \times \eta_{TTC}$, where η_{STT} is solar-to-thermal efficiency, and η_{TTC} is thermal-to-chemical efficiency. Ideally, $\eta_{TTC} = \Delta G_{1298K}/\Delta H_{solid}$, where ΔG_{1298K} (~256 $kJ\cdot(0.5\ mol\ O_2)^{-1}$) is the change in the Gibbs free energy at 298 K for CO_2 thermolysis (Reaction 1). By assuming an achievable η_{STT} of 70%, a target η_{TTC} of 28.6% is required to achieve a practical η_{STC} of 20%, which is competitive to the technology that a solar photovoltaic device coupled with an electrolyser[27]. Miller, *et al.*[2] analysed that potential redox materials should be able to achieve a theoretical thermal-to-chemical efficiency which is twice of the target η_{TTC} (Eq. (6)).

$$\Delta H_{solid} \leqslant 450\ kJ\cdot(0.5\ mol\ O_2)^{-1} \quad (6)$$

Therefore, Eq. (4) to (6) were used to calculate the boundary values of (ΔS_{solid}, ΔH_{solid}). Eq. (4) and (5) tell that the (ΔS_{solid}, ΔH_{solid}) boundary varies with operating temperatures (T_H and T_L) and operating pressure (P_{O_2}). For the thermal reduction step of a practical solar thermochemical reactor, T_H=2000 K[18] and P_{O_2}=0.101 kPa[2]

were used as the upper limit for the reduction temperature and the lower limit for the pressure respectively. For the oxidation step, the exothermic reaction is thermodynamically favorable for low temperatures, but suffers from slow kinetics. Thus, T_L of 1000 K[18] was used as the lower limit for the oxidation temperature. Now, the criteria is summarized as Eq. (7) with the descriptors, ΔS_{solid} and ΔH_{solid}, defined in Eq. (3).

$$
\begin{cases}
\Delta H_{solid} \leqslant 450 \text{ kJ} \cdot (0.5 \text{ mol O}_2)^{-1} \\
\Delta H_{solid} \leqslant T_H \left(\Delta S_{solid} + \frac{1}{2} S_{O_2, T_H} - \frac{1}{2} R \ln P_{O_2} \right) \\
\quad \text{at } T_H = 2000 \text{ K and } P_{O_2} = 0.101 \text{ kPa} \\
\Delta H_{solid} \geqslant (\Delta H_{f, CO, T_L} - \Delta H_{f, CO_2, T_L}) - \\
\quad T_L (S_{CO, T_L} - S_{CO_2, T_L} - \Delta S_{solid}), \text{ at } T_L = 1000 \text{ K}
\end{cases}
\tag{7}
$$

As shown in Fig. 1, the (ΔS_{solid}, ΔH_{solid}) area below the purple curve features theoretical thermal-to-chemical efficiency which is twice higher than the target. (ΔS_{solid}, ΔH_{solid}) below the green curve and above the blue curve are thermodynamically favorable for thermal reduction step (Reaction (2)) and CO₂ splitting step (Reaction (3)) respectively. Therefore, the combination of ΔS_{solid} and ΔH_{solid} of qualified redox material should fall in the shaded triangular region.

These results highlight the importance of accurate predictions of ΔS_{solid} and ΔH_{solid}, which are investigated in Section 2. Fig. 1 also shows that a positive ΔS_{solid} opens the favorable region, so redox materials with large positive ΔS_{solid} benefits reaction thermodynamics. However, this is non-trivial for redox materials in the stoichiometric regime, because the reduced oxide has fewer atoms and thereby, fewer vibrational degrees of freedom.
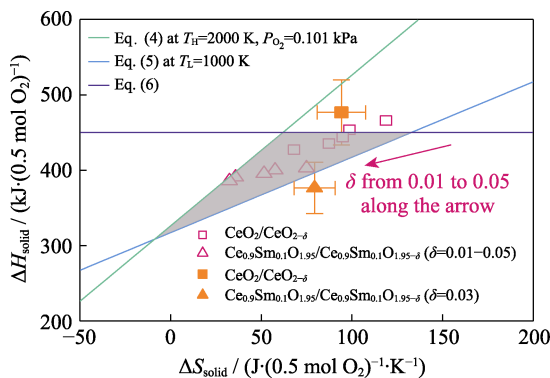

Fig. 1　Thermodynamic assessment map
The combination of ΔS_{solid} and ΔH_{solid} of redox material candidates should fall in the shaded triangular region. The experimental data points (open scatters) of (ΔS_{solid}, ΔH_{solid}) were plotted for pure $CeO_2/CeO_{2-\delta}$ and 10% Samaria-doped $Ce_{0.9}Sm_{0.1}O_{1.95}/Ce_{0.9}Sm_{0.1}O_{1.95-\delta}$ redox pairs (δ=0.01–0.05)[28-29]. The calculation results (solid scatters) in Section 2 were also plotted for these redox pairs (δ=0.03). Error bars represent standard deviations. Colourful figure is available on website

Fig. 1 plots the experimental data[28-29] of (ΔS_{solid}, ΔH_{solid}) for pure $CeO_2/CeO_{2-\delta}$ and 10% Samaria-doped $Ce_{0.9}Sm_{0.1}O_{1.95}/Ce_{0.9}Sm_{0.1}O_{1.95-\delta}$ redox pairs (δ=0.01–0.05) as well. Results show that ΔS_{solid}, ΔH_{solid} of both pure and doped ceria fall in the favorable region except for the pure ceria redox pair with δ=0.01. These results are reasonable because pure and doped ceria are usually used as benchmark redox materials in literature[5-8].

The favorable region varies with operating temperature and pressure as shown in Fig. 2. Therefore, it is important to recognize that the developed thermodynamic framework can further be used for reactor testing to design optimal operating condition of a specific qualified redox pair. For example, results show that thermodynamically favorable thermal reduction step (Reaction (2)) can be performed at lower temperatures (Fig. 2(a)) and higher pressures (Fig. 2(b)) for pure and doped ceria redox pairs with larger ΔS_{solid} (smaller δ). These milder operating conditions can significantly reduce thermal radiation loss and reactor design complexity.
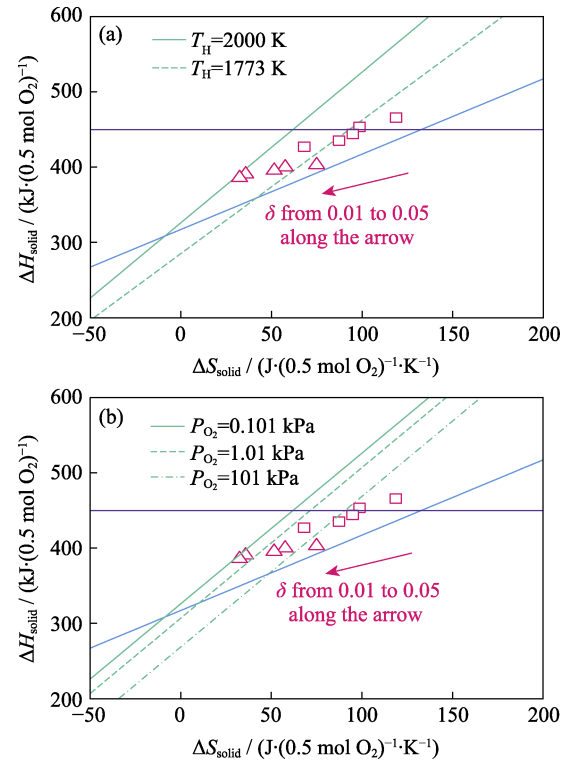

Fig. 2　Variations of the favorable regions with operating conditions of the thermal reduction step (Reaction (2))
(a) Temperature. T_H=2000 and 1773 K; (b) Pressure. P_{O_2}=0.101, 1.01 and 101 kPa. Other conditions in (a, b) are the same with those in Fig. 1; Colourful figure is available on website

2　First-principles predictions of descriptors

In this section, first-principles calculations were applied to the predictions of the descriptors (ΔS_{solid}, ΔH_{solid}) so that new redox materials can be added to the thermody-

namic assessment map of Fig. 1.

In the first step, fast and reasonable predictions of (ΔS_{solid}, ΔH_{solid}) were demonstrated. ΔS_{solid} in Eq. (8) includes both vibrational (ΔS_{vib}) and configurational (ΔS_{conf}) entropic contributions[25].

$$\Delta S_{solid} = \Delta S_{vib} + \Delta S_{conf} \quad (8)$$

Vibrational entropic contributions originate from the formations of defects, including oxygen vacancies as well as polarons[28,30], during the partial reduction step (Reaction (4)).

$$2Ce_{Ce}^{\times} + O_O^{\times} \rightarrow V_O^{\bullet\bullet} + 2Ce_{Ce}' + \frac{1}{2}O_2 \quad (Reaction (4))$$
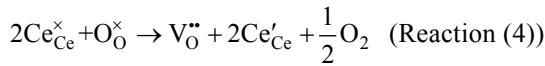
where $Ce_{Ce}^{\times}$ and $O_O^{\times}$ represent Ce and O ions on their respective sites, $V_O^{\bullet\bullet}$ is a doubly ionized oxygen vacancy, and Ce_{Ce}' is an electron localized on a Ce ion, *i.e.* polaron. Therefore, ΔS_{vib} is expressed in Eq. (9).

$$\Delta S_{vib} = \Delta S_{V_O^{\bullet\bullet}} + 2\Delta S_{Ce_{Ce}'} = (S_{V_O^{\bullet\bullet}} - S_{bulk}) + 2(S_{Ce_{Ce}'} - S_{bulk}) \quad (9)$$

Where S_{bulk}, $S_{V_O^{\bullet\bullet}}$ and $S_{Ce_{Ce}'}$ are the entropies of a bulk CeO_2 supercell (Fig. 3(a)), a CeO_2 supercell with a single oxygen-vacancy defect (Fig. 3(b)) and a CeO_2 supercell with a single polaron defect (Fig. 3(c)), taking pure CeO_2 as an example. More details are available in Supporting Materials on the preparations of the supercells and on the calculations of S_{bulk}, $S_{V_O^{\bullet\bullet}}$, $S_{Ce_{Ce}'}$ and corresponding ΔS_{vib}.

Configurational entropic contributions are from the random distributions of ionic (oxygen vacancies) and electronic (polarons) defects, so ΔS_{conf} was calculated using the ideal solution model (Methods in Supporting Materials).
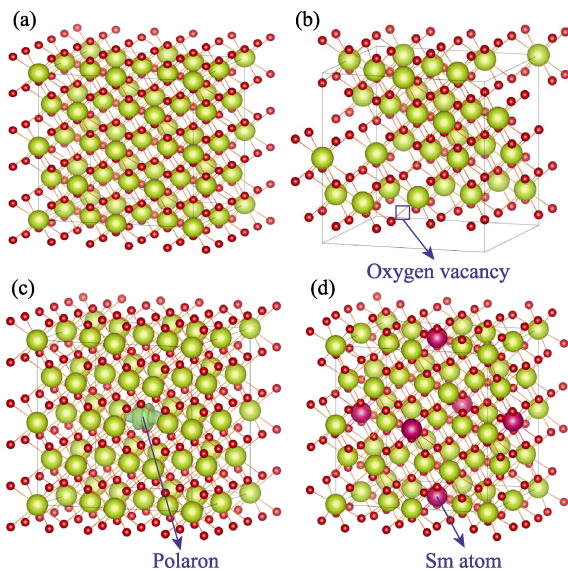

Fig. 3　Supercells for DFT+U calculations
(a) Bulk CeO_2 supercell; (b) CeO_2 supercell with a single oxygen-vacancy defect; (c) CeO_2 supercell with a single polaron defect(The charge density of the polaron is also shown); (d) Sm-doped CeO_2 supercell (Methods in Supporting Materials)

ΔH_{solid} was approximated as the oxygen-vacancy formation energy[11,21].

ΔS_{vib}, ΔS_{conf} and ΔH_{solid} of the $CeO_2/CeO_{2-\delta}$ and $Ce_{0.9}Sm_{0.1}O_{1.95}/Ce_{0.9}Sm_{0.1}O_{1.95-\delta}$ redox pairs ($\delta=0.03$) were calculated before the comparison of these calculation results with experimentally measured ΔS_{solid} and ΔH_{solid}[28-29,31]. Table 1 shows that this applied theoretical method can predict ΔS_{solid} and ΔH_{solid} of pure and Sm-doped ceria pairs, and expectedly other redox materials with reasonable accuracy. Particularly for ΔS_{solid} of the $CeO_2/CeO_{2-\delta}$ redox pair ($\delta=0.03$), it was demonstrated that the relative differences between calculated and measured values are below 12%, although it is found in references[20, 23] that this method might over-estimate ΔS_{solid}. Regarding ΔH_{solid} of pure and Sm-doped ceria pairs ($\delta=0.03$), the relative differences are also below 12%, demonstrating sufficient accuracy of this method which is expected to be more efficient enabled by the advancement and power of high-throughput computational tools[15-16].

Table 1　Comparison between calculated and measured values of ΔS_{solid} and ΔH_{solid}

Redox pair	Ref.	ΔS_{vib}^{a}	ΔS_{conf}^{a}	ΔS_{solid}^{a}	ΔH_{solid}^{a}
$CeO_{2-\delta}$ ($\delta=0.03$)	Experimental[28]	–	–	~91.2^b	~429
	Experimental[31]	–	–	~105.9^b	~441
	This work	13.7	80.5	94.2	476.7
$Ce_{0.9}Sm_{0.1}O_{1.95-\delta}$ ($\delta=0.03$)	Experimental[29]	–	–	~67.7^b	~400
	This work	9.1	70.3	79.4	376.5

^{a} Entropy and enthalpy units are J·(0.5 mol O_2)$^{-1}$·K^{-1} and kJ·(0.5 mol O_2)$^{-1}$; ^{b} Obtained from measured reduction entropy minus $0.5S_{O_2}$

Then physical insights were given into these calculation results to further demonstrate the reliability of the applied theoretical method. Fig. 4 shows the variations of $\Delta S_{V_O^{\bullet\bullet}}$, $2\Delta S_{Ce_{Ce}'}$, ΔS_{vib} and ΔS_{solid} with temperatures. Since the results for pure and Sm-doped ceria pairs follow the same trend, the $CeO_2/CeO_{2-\delta}$ redox pair is taken as an example. It is observed that $\Delta S_{V_O^{\bullet\bullet}}$ is negative, which can be intuitively understood from less atoms and resultantly lower vibrational degrees of freedom of the reduced oxides. This can also be quantitatively explained by a negative relaxation volume, ΔV_{rel}, due to the formation of an oxygen-vacancy defect, from Eq. (S2) in Supporting Materials. The surrounding O ions relax towards the vacancy for a distance longer than the Ce ions relax away, which renders a relaxation volume of –0.0170 nm^3 (Table S1). On the contrary, $2\Delta S_{Ce_{Ce}'}$ is positive, which is resultant from a positive relaxation volume ($\Delta V_{rel}=0.0139$ nm^3). These results indicate that the change of volume, due to the formation of defects, dominates vibrational entropic contribution. The calculated ΔS_{vib} is 13.5 J·(0.5 mol O_2)$^{-1}$·K^{-1}
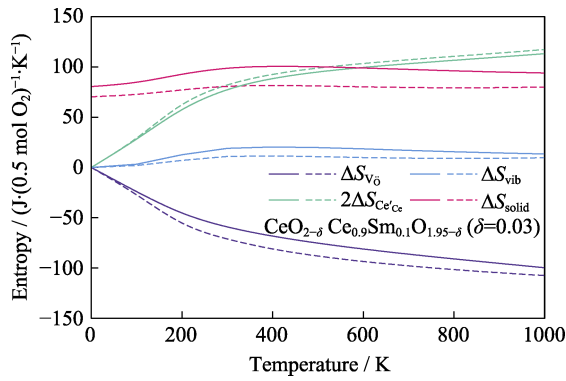
Fig. 4　Variations of $\Delta S_{V_{\ddot{O}}}$, $2\Delta S_{Ce'_{Ce}}$, ΔS_{vib}, and ΔS_{solid} with temperature

Solid and dash curves are for CeO$_2$/CeO$_{2-\delta}$ and Ce$_{0.9}$Sm$_{0.1}$O$_{1.95}$/Ce$_{0.9}$Sm$_{0.1}$O$_{1.95-\delta}$ redox pairs (δ=0.03), respectively; Colourful figure is available on website

at 1000 K which agrees well with the experimental data[28], and the calculated ΔS_{conf} is 80.5 J·(0.5 mol O$_2$)$^{-1}$·K^{-1}. For the Ce$_{0.9}$Sm$_{0.1}$O$_{1.95}$/Ce$_{0.9}$Sm$_{0.1}$O$_{1.95-\delta}$ redox pair, the fact that ΔS_{conf} (70.3 J·(0.5 mol O$_2$)$^{-1}$·K^{-1}) is smaller than that of pure ceria redox pair is reasonable because doping by an atom with a lower valence renders a reduction of possible microscopic states. ΔS_{solid} are 94.0 and 79.4 J·(0.5 mol O$_2$)$^{-1}$·K^{-1} for the CeO$_2$/CeO$_{2-\delta}$ and the Ce$_{0.9}$Sm$_{0.1}$O$_{1.95}$/Ce$_{0.9}$Sm$_{0.1}$O$_{1.95-\delta}$ redox pairs (δ=0.03). These values are comparable to 0.5S_{O_2}(121.8 J·(0.5 mol O$_2$)$^{-1}$·K^{-1}) at 1000 K. These high positive ΔS_{solid}, attributed to the configurational and polaron defective entropic contributions, explain the excellent thermochemical performance of pure and doped ceria reported in literature [5-8].

3　Discussion

Based on the results of this work, a viable screening approach of materials for solar-driven CO$_2$ splitting using two-step thermochemical cycles was proposed as shown in Fig. 5.

The first step is to calculate the descriptors, the combination of ΔS_{solid} and ΔH_{solid} defined in Eq. (3) by the developed DFT+U based first-principles approach. As described in Introduction, despite the recognition of the entropic effect, energy descriptors (enthalpy of formation

or energy of oxygen-vacancy formation) were usually used for the screening of material candidates in literature [11-12, 22]. Therefore, (ΔS_{solid}, ΔH_{solid}) represents a more general descriptor.

The second step is to screen material candidates by the derived criteria defined in Eq. (7) and find out qualified redox materials. As described in Section 1, these criteria were derived by comprehensively considering non-stoichiometric reaction mechanism, theoretical efficiency and practical operating conditions. It has to be pointed out that materials with (ΔS_{solid}, ΔH_{solid}) near the boundary of the favorable region (Fig. 1) should also be screened as qualified redox materials considering the accuracy of DFT calculations. In addition, Eq. (6) varies with target solar-to-chemical and thermal-to-chemical efficiencies as well as achievable solar-to-thermal efficiency. For example, ΔH_{solid} is $\leqslant$ 600 kJ·(0.5 mol O$_2$)$^{-1}$ in Eq. (6) with the target solar-to-chemical efficiency reseted from 20% to 15%. Resultantly, the solid square scatter is inside the favorable region.

The third step is to perform reactor testing using qualified redox material. Thermodynamics of redox material candidates represents an initial screening criterion[23,32], which was demonstrated in this work. Reaction kinetics of redox material candidates, which is characterized in reactor testing, is the important subsequent criterion[33-34], although reaction kinetics is out of the scope of this work.

4　Conclusions

In summary, this work presented a rationale for thermodynamic and first-principles assessments of redox materials for solar-driven CO$_2$ splitting using two-step thermochemical cycles. The combination of solid-state change of entropy (ΔS_{solid}) and enthalpy of formation (ΔH_{solid}) was used as the descriptor. Comprehensive criteria based on it were derived to obtain the (ΔS_{solid}, ΔH_{solid}) map. It was found that a triangular region in this map identified qualified material candidates featuring large positive ΔS_{solid} and small enough ΔH_{solid}. Furthermore, a DFT+U based
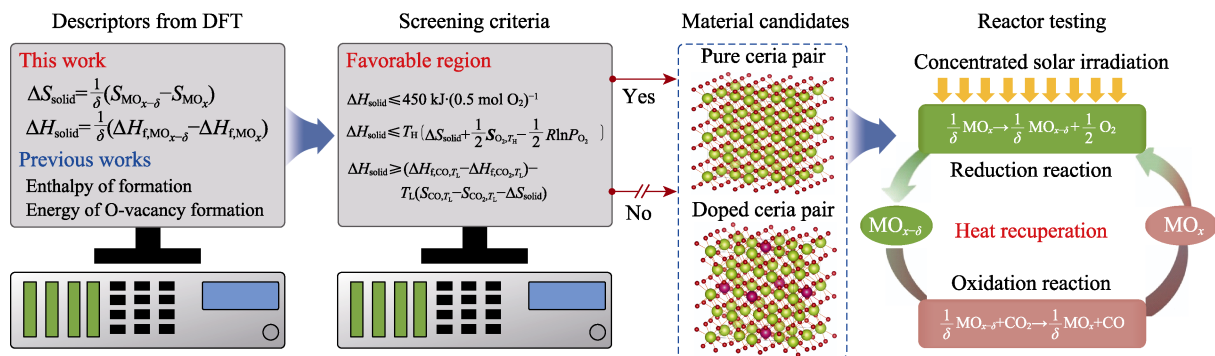

Fig. 5　Illustration of a viable screening approach

first-principles approach was developed to fast and reasonably predict ΔS_{solid} and ΔH_{solid} for redox materials without available thermochemical data. This rationale was exemplified for pure and samaria-doped ceria.

Acknowledgments

Supporting materials

Supporting materials related to this article can be found at https://doi.org/10.15541/jim20210164.

References:

[1] LU Y, ZHU L, AGRAFIOTIS C, *et al.* Solar fuels production: two-step thermochemical cycles with cerium-based oxides. *Prog. Energ. Combust. Sci.*, 2019, **75:** 100785.

[2] MILLER J, MCDANIEL A, ALLENDORF M. Considerations in the design of materials for solar-driven fuel production using metal-oxide thermochemical cycles. *Adv. Energy Mater.*, 2014, **4:** 1300469.

[3] HAO Y, ZOU W, AN R. Let the sun shine into a brighter future: an interview with Prof. Aldo Steinfeld. *Sci. Bull.*, 2017, **62:** 1102–1103.

[4] ABANADES S, CHARVIN P, FLAMANT G, *et al.* Screening of water-splitting thermochemical cycles potentially attractive for hydrogen production by concentrated solar energy. *Energy*, 2006, **31:** 2805–2822.

[5] MARXER D, FURLER P, TAKACS M, *et al.* Solar thermochemical splitting of CO_2 into separate streams of CO and O_2 with high selectivity, stability, conversion, and efficiency. *Energ. Environ. Sci.*, 2017, **10:** 1142–1149.

[6] HAO Y, YANG C K, HAILE S M. Ceria-zirconia solid solutions ($Ce_{1-x}Zr_xO_2$-delta, $x \leqslant 0.2$) for solar thermochemical water splitting: a thermodynamic study. *Chem. Mater.*, 2016, **26:** 6073–6082.

[7] GRIESHAMMER S, MARTIN M. Influence of defect interactions on the free energy of reduction in pure and doped ceria. *J. Mater. Chem. A*, 2017, **5:** 9241–9249.

[8] BULFIN B, CALL F, LANGE M, *et al.* Thermodynamics of CeO_2 thermochemical fuel production. *Energ. Fuel*, 2015, **29:** 1001–1009.

[9] MUHICH C L, EVANKO B W, WESTON K C, *et al.* Efficient generation of H_2 by splitting water with an isothermal redox cycle. *Science*, 2013, **341:** 540–542.

[10] Al-SHANLITI I A, BAYON A, WEIMER A W. Reduction kinetics of hercynite redox materials for solar thermochemical water splitting. *Chem. Eng. J.*, 2020, **389:** 124429.

[11] MUHICH C L, EHRHART B D, WITTE V A, *et al.* Predicting the solar thermochemical water splitting ability and reaction mechanism of metal oxides: a case study of the hercynite family of water splitting cycles. *Energ. Environ. Sci.*, 2015, **8:** 3687–3699.

[12] BORK A H, POVODEN-KARADENIZ E, RUPP J L. Modeling thermochemical solar-to-fuel conversion: CALPHAD for thermodynamic assessment studies of perovskites, exemplified for (La,Sr)MnO_3. *Adv. Energy Mater.*, 2017, **7:** 1601086.

[13] FU M, WANG L, MA T, *et al.* Mechanism of CO production around oxygen vacancy of $LaMnO_3$: an efficient and rapid evaluation of the doping effect on the kinetics and thermodynamic driving force

of CO_2-splitting. *J. Mater. Chem. A*, 2020, **8:** 1709–1716.

[14] WANG L, MA T, DAI S, *et al.* Experimental study on the high performance of Zr doped $LaCoO_3$ for solar thermochemical CO production. *Chem. Eng. J.*, 2020, **389:** 124426.

[15] BARTEL C J, RUMPTZ J R, WEIMER A W, *et al.* High-throughput equilibrium analysis of active materials for solar thermochemical ammonia synthesis. *ACS Appl. Mater. Inter.*, 2019, **11:** 24850–24858.

[16] EMERY A A, SAAL J E, KIRKLIN S, *et al.* High-throughput computational screening of perovskites for thermochemical water splitting applications. *Chem. Mater.*, 2016, **28:** 5621–3564.

[17] GAUTAM G S, CARTER E A. Evaluating transition-metal oxides within DFT-SCAN and SCAN+U frameworks for solar thermochemical applications. *Phys. Rev. Mater.*, 2018, **2:** 095401.

[18] MEREDIG B, WOLVERTON C. First-principles thermodynamic framework for the evaluation of thermochemical H_2O– or CO_2-splitting materials. *Phys. Rev. B*, 2009, **80:** 308–310.

[19] SHAH P R, KIM T, ZHOU G, *et al.* Evidence for entropy effects in the reduction of ceria-zirconia solutions. *Chem. Mater.*, 2006, **18:** 5363–5369.

[20] NAGHAVI S S, EMERY A A, HANSEN H, *et al.* Giant onsite electronic entropy enhances the performance of ceria for water splitting. *Nat. Commun.*, 2017, **8:** 285.

[21] ONG M, CAMPBELL Q, DABO I, *et al.* First-principles investigation of $BiVO_3$ for thermochemical water splitting. *Int. J. Hydrogen Energ.*, 2019, **44:** 1425–1430.

[22] MICHALSKY R, BOTU V, HARGUS C M, *et al.* Design principles for metal oxide redox materials for solar-driven isothermal fuel production. *Adv. Energy Mater.*, 2015, **5:** 1401082.

[23] GOPAL C B, VAN DE WALLE A. *Ab initio* thermodynamics of intrinsic oxygen vacancies in ceria. *Phys. Rev. B*, 2012, **86:** 5505–5511.

[24] ZACHERLE T, SCHRIEVER A, DE SOUZA R A, *et al. Ab initio* analysis of the defect structure of ceria. *Phys. Rev. B*, 2013, **87:** 134104.

[25] GRIESHAMMER S, ZACHERLE T, MARTIN M. Entropies of defect formation in ceria from first principles. *Phys. Chem. Chem. Phys.*, 2013, **15:** 15935–15942.

[26] CHASE M W. NIST-JANAF Thermochemical Tables, 4th Edition. New York: American Institute of Physics, 1998**:** 647–1745.

[27] CHENG W H, RICHTER M H, SULLIVAN I, *et al.* CO_2 reduction to CO with 19% efficiency in a solar-driven gas diffusion electrode flow cell under outdoor solar illumination. *ACS Energy Lett.*, 2020, **5:** 470–476.

[28] PANLENER R J, BLUMENTHAL R N, GARNIER J E. A thermodynamic study of nonstoichiometric cerium dioxide. *J. Phys. Chem. Solids*, 1975, **36:** 1213–1222.

[29] KOBAYASHI T, WANG S, DOKIYA M, *et al.* Oxygen nonstoichiometry of $Ce_{1-y}Sm_yO_{2-0.5y-x}$ (y=0.1, 0.2). *Solid State Ionics*, 1999, **126:** 349–357.

[30] KEATING P R L, SCANLON D O, MORGAN B J, *et al.* Analysis of intrinsic defects in CeO_2 using a Koopmans-like GGA+U approach. *J. Phys. Chem. C*, 2012, **116:** 2443–2452.

[31] BULFIN B, HOFFMANN, L, DE OLIVEIRA L, *et al.* Statistical thermodynamics of non-stoichiometric ceria and ceria zirconia solid solutions. *Phys. Chem. Chem. Phys.*, 2016, **18:** 23147–23154.

[32] DAVENPORT T C, YANG C K, KUCHARCZYK C J, *et al.* Implications of exceptional material kinetics on thermochemical fuel production rates. *Energy Technol.*, 2016, **4:** 764–770.

[33] DAVENPORT T C, KEMEI M, IGNATOWICH M J, *et al.* Interplay of material thermodynamics and surface reaction rate on the kinetics of thermochemical hydrogen production. *Int. J. Hydrogen Energ.*, 2017, **42:** 16932–16945.

[34] BULFIN B, LOWE A J, KEOGH K A, *et al.* An analytical model of CeO_2 oxidation and reduction. *J. Phys. Chem. C*, 2013, **117:** 24129–24137.

太阳能驱动的两步热化学循环二氧化碳裂解反应
活性材料的热力学与第一性原理评价

冯清影, 刘 东, 张 莹, 冯 浩, 李 强

(南京理工大学 能源与动力工程学院, 南京 210094)

摘 要: 太阳能驱动两步热化学循环裂解二氧化碳可制备碳中性燃料, 为替代化石燃料、缓解全球变暖提供了技术途径。新型活性材料的开发对该技术非常重要。已有研究通常采用能量描述符(材料生成焓或氧空位生成能)评价候选材料, 忽略了材料熵的重要性。本研究采用活性材料的熵和生成焓的组合作为描述符, 提出评价准则, 开展材料可行性的热力学分析。结果表明, 活性材料应兼具较大的正的熵变与较小的生成焓变。在此基础上, 本研究以氧化铈和钐掺杂的氧化铈为例, 发展了基于第一性原理的活性材料熵和生成焓的计算方法, 为新型材料的筛选与开发提供基础。计算结果揭示了极化子振动熵以及氧空位和极化子构型熵对活性材料熵变的贡献。

关 键 词: 二氧化碳裂解; 两步热化学循环; 第一性原理; 熵; 太阳能制燃料

中图分类号: TK51   **文献标志码:** A

Supporting materials:

Thermodynamic and First-principles Assessments of Materials for Solar-driven CO₂ Splitting Using Two-step Thermochemical Cycles

FENG Qingying, LIU Dong, ZHANG Ying, FENG Hao, LI Qiang

(School of Energy and Power Engineering, Nanjing University of Science and Technology, Nanjing 210094, China)

Methods

General setups of first-principles calculations All first-principles density functional theory (DFT) calculations were performed using the Vienna *Ab-initio* Simulation Package (VASP)[S1] where the Perdew-Burke Ernzerhof (PBE)[S2] generalized gradient approximation (GGA) and the projector augmented wave (PAW)[S3] method were used. The wave functions were expanded in plane waves with 500 eV energy cut-off. The 2×2×2 Monkhorst-Pack mesh was used for k-point sampling. Convergence parameters of 10^{-8} eV and 10^{-3} eV·nm^{-1} were used for the relaxation of electrons and ions respectively. The $5s^2 5p^6 6s^2 5d^1 4f^1$ electrons were treated as the valence electrons for Ce with $2s^2 2p^4$ for O and $5s^2 5p^6 6s^2 5d^1$ for Sm. The $+U$ approach ($U=5$ eV) was employed to describe the localized 4f-orbitals of Ce[S4]. Sm has six f-electrons, so its localized f-electrons was treated with the standard model in GGA potential where five f-electrons were placed in the core (Sm adopts a valency of 3 in doped ceria)[S5].

Preparations of bulk and defective supercells All 2×2×2 fluorite supercells contain 96 lattice positions (Fig. 3). For defective supercells, the number of electrons was set corresponding to their charge states. The method reported by Zacherle, *et al.*[S6] was used to prepare the defective supercell with a single polaron (Fig. 3(c)). For the 10% Sm-doped ceria supercell (Fig. 3(d)), Sm atoms were placed symmetrically to reduce computational costs. The effect of random distribution was included in the calculations of $\Delta S_{\text{conf.}}$. For all supercells, imaginary frequencies were not observed in their phonon dispersion demonstrating the stability of these structures. Fig. S1 exhibits representative phonon dispersion results of a 10% Sm-doped ceria supercell comprising an oxygen vacancy. The calculated lattice constant of ceria is 0.5499 nm, which agrees well with the experimental value of 0.5411 nm[S7], and with the one (0.5494 nm) calculated using GGA+U method[S6]. The slight difference from the experimental value is due to intrinsic overestimation of lattice constants by GGA+U method[S6].

Phonon calculations The vibrational entropy of each supercell (Eq. (9)) was expressed as Eq. (S1) using the harmonic approximation.

$$S_{\text{bulk}/\text{V}_{\text{O}}^{\cdot\cdot}/\text{Ce}'_{\text{Ce}}} = Nk_{\text{B}} \int_0^\infty \left\{ \frac{\hbar\omega}{2k_{\text{B}}T} \coth\left(\frac{\hbar\omega}{2k_{\text{B}}T}\right) - \ln\left[2\sin h\left(\frac{\hbar\omega}{2k_{\text{B}}T}\right)\right]\right\} g(\omega)\mathrm{d}\omega \tag{S1}$$

where, N is the number of degrees of freedom, k_{B} is the Boltzmann constant, $\hbar$ is the Planck constant, T is the temperature. The normalized phonon density of states, $g(\omega)$, at each phonon frequency, ω, was calculated using the open source package of Phonopy[S8]. Phonon calculations were performed for constant volume conditions ($V=V_0$) where the stress is not relaxed due to defect formation, while entropies for constant pressure conditions ($p=p_0$) in Eq. (9) were more concerned experimentally. They were obtained by Eq. (S2)[S9].

$$\Delta S_{\text{V}_{\text{O}}^{\cdot\cdot}/\text{Ce}'_{\text{Ce}}}(p=p_0) = \Delta S_{\text{V}_{\text{O}}^{\cdot\cdot}/\text{Ce}'_{\text{Ce}}}(V=V_0) + \alpha_{\text{V}} K_{\text{T}} \Delta V_{\text{rel}} \tag{S2}$$

where α_{V} is the volumetric thermal expansion coefficient, K_{T} is the isothermal bulk modulus and ΔV_{rel} is the relaxation volume, *i.e.*, the difference between the volume of a defective supercell (oxygen-vacancy or polaron) and that of a bulk supercell. The free energy (E) of 11 unit cells with volumes (V) ranging from 0.03656 nm^3 to 0.04656 nm^3 was calculated for each temperature. These E-V curves for each temperature were fitted using the Birch-Murnaghan equation(Eq. (S3))[S9] to obtain K_{T} and equilibrium volumes (V_0) for each temperature.

$$E(V) = E_0 + \frac{9V_0 K_{\text{T}}}{16}\left\{\left[\left(\frac{V_0}{V}\right)^{\frac{2}{3}} - 1\right]^3 K_{\text{T}}' + \left[\left(\frac{V_0}{V}\right)^{\frac{2}{3}} - 1\right]^2\left[6 - 4\left(\frac{V_0}{V}\right)^{\frac{2}{3}}\right]\right\} \tag{S3}$$

Then, α_{V} was derived from equilibrium volumes as Eq. (S4).

$$\alpha_{\text{V}} = \frac{1}{V_0}\left(\frac{\partial V_0}{\partial T}\right)_p \tag{S4}$$

Calculated α_V, K_T and ΔV_{rel} are available in Fig. S2 and Table S1.

Calculations of configurational entropic contributions

ΔS_{conf} was calculated using the ideal solution model. For a general $Ce_{1-y}Sm_yO_{2-0.5y}/Ce_{1-y}Sm_yO_{2-0.5y-\delta}$ redox pair, ΔS_{conf} was calculated as Eq. (S5)[S10].

$$\Delta S_{conf} = -R \ln \left[\frac{0.5y + \delta}{2 - 0.5y - \delta} \left(\frac{2\delta}{1 - y - 2\delta} \right)^2 \right] \quad (S5)$$
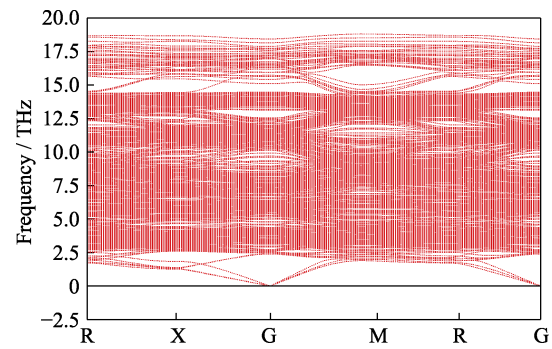
Supporting figures and tables

Fig. S1   Phonon dispersion of a 10% samaria-doped ceria supercell comprising an oxygen vacancy
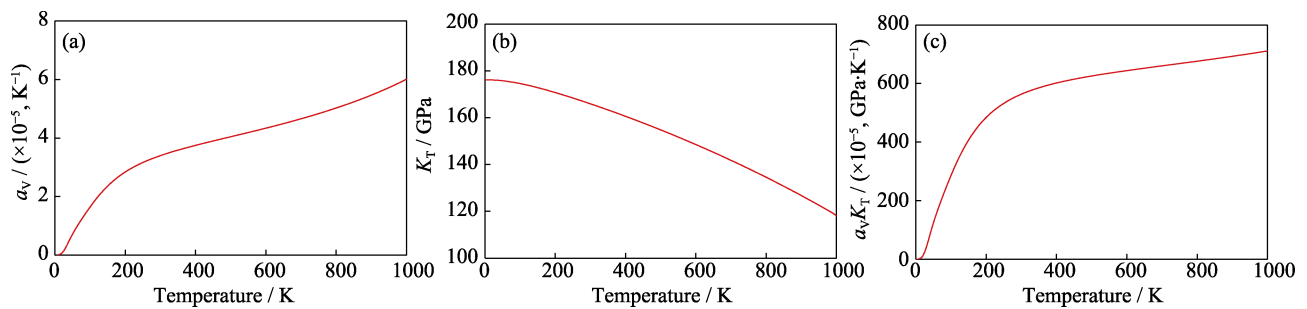

Fig. S2   Calculated variations of (a) α_V, (b) K_T and (c) $\alpha_V \times K_T$ with temperatures

Table S1   Relaxation volumes due to formations of an oxygen vacancy and a polaron for $CeO_{2-\delta}$ and $Ce_{0.9}Sm_{0.1}O_{1.95-\delta}$

Oxide	$\Delta V_{rel, vacancy}$/ nm^3	$\Delta V_{rel, polaron}$/nm^3
$CeO_{2-\delta}$	−0.0170	0.0139
$Ce_{0.9}Sm_{0.1}O_{1.95-\delta}$	−0.0170	0.0144

References:

[1] KRESSE G, FURTHMULLER J. Efficient iterative schemes for *ab initio* total-energy calculations using a plane-wave basis set. *Phys. Rev. B*, 1996, **54**: 11169–11186.

[2] PERDEW J P, BURKE K, ERNZERHOF M. Generalized gradient approximation made simple. *Phys. Rev. Lett.*, 1997, **78**: 18–28.

[3] BLOCHL P E. Projector augmented-wave method. *Phys. Rev. B*, 1994, **50**: 17953–17979.

[4] DUDARV S L, BOTTON G A, SAVRASOV S Y, *et al.* Electron-energy-loss spectra and the structural stability of nickel oxide: an LSDA+U study. *Phys. Rev. B*, 1998, **57**: 1505–1509.

[5] KOETTGEN J, GRIESHAMMER S, HEIN P, *et al.* Understanding the ionic conductivity maximum in doped ceria: trapping and blocking. *Phys. Chem. Chem. Phys.*, 2018, **20**: 14291–14321.

[6] ZACHERLE T, SCHRIEVER A, DE SOUZA R A, *et al. Ab initio* analysis of the defect structure of ceria. *Phys. Rev. B*, 2013, **87**: 134104.

[7] GERWARD L, STAUN OLSEN J, PETIT L, *et al.* Bulk modulus of CeO$_2$ and PrO$_2$-an experimental and theoretical study. *J. Alloy Compd.*, 2005, **400**: 56–61.

[8] GINZE X, LEE C. Dynamical matrices, born effective charges, dielectric permittivity tensors, and interatomic force constants from density-functional perturbation theory. *Phys. Rev. B*, 1997, **55**: 10355–10368.

[9] GRIESHAMMER S, ZACHERLE T, MARTIN M. Entropies of defect formation in ceria from first principles. *Phys. Chem. Chem. Phys.*, 2013, **15**: 15935–15942.

[10] KOBAYASHI T, WANG S, DOKIYA M, *et al.* Oxygen nonstoichiometry of Ce$_{1-y}$Sm$_y$O$_{2-0.5y-x}$ (*y*=0.1, 0.2). *Solid State Ionics*, 1999, **126**: 349–357.